



# Construction of Z-scheme Cu<sub>2</sub>O/Cu/AgBr/Ag photocatalyst with enhanced photocatalytic activity and stability under visible light



J. He<sup>a</sup>, D.W. Shao<sup>a</sup>, L.C. Zheng<sup>a</sup>, L.J. Zheng<sup>a</sup>, D.Q. Feng<sup>a</sup>, J.P. Xu<sup>b</sup>, X.H. Zhang<sup>c</sup>, W.C. Wang<sup>a</sup>, W.-H. Wang<sup>a</sup>, F. Lu<sup>a</sup>, H. Dong<sup>a</sup>, Y.H. Cheng<sup>a,d,\*</sup>, H. Liu<sup>a,\*\*</sup>, R.K. Zheng<sup>d</sup>

<sup>a</sup> Department of Electronics and Key Laboratory of Photo-Electronic Thin Film Devices and Technology of Tianjin, Nankai University, Tianjin 300350, China

<sup>b</sup> Institute of Material Physics, Key Laboratory of Display Materials and Photoelectric Devices, Ministry of Education, Tianjin University of Technology, Tianjin 300384, China

<sup>c</sup> School of Material Science and Engineering, Hebei University of Technology, Tianjin 300130, China

<sup>d</sup> School of Physics, The University of Sydney, NSW 2006, Australia

## ARTICLE INFO

### Article history:

Received 20 June 2016

Received in revised form

20 September 2016

Accepted 31 October 2016

Available online 2 November 2016

### Keywords:

Visible light photocatalysis

Cu<sub>2</sub>O/Cu/AgBr/Ag

Photodegradation stability

Z-scheme mechanism

## ABSTRACT

A series of Cu<sub>2</sub>O/Cu/AgBr/Ag photocatalysts were synthesized by a redox procedure followed by photo-assisted deposition. X-ray diffraction (XRD), scanning electron microscopy (SEM), transmission electron microscopy (TEM) and X-ray photoelectron spectroscopy (XPS) were utilized to characterize the structure of the system. It is found that Cu nanoparticles (NPs) could be controllable to grow in between Cu<sub>2</sub>O and AgBr. Without Cu NPs between Cu<sub>2</sub>O/AgBr, under visible light irradiation for 50 min, only a low photocatalytic degradation of methyl orange (MO) (~51%) was observed compared with the high MO photodegradation (~98%) in the presence of Cu NPs. Furthermore, introducing Cu NPs assists in accelerating excited carrier transfer at the interface between Cu<sub>2</sub>O and AgBr, measured by the photoluminescence spectra, photocurrent and electrochemical impedance spectra, which thus helps to increase the stability of the photocatalyst. The increased photocatalytic activity and stability can be attributed to the favorable band alignment between Cu<sub>2</sub>O and AgBr mediated by Cu NPs, which is known as the Z-scheme mechanism and confirmed by the detection of the active species. These results demonstrate that the Cu<sub>2</sub>O/Cu/AgBr/Ag is a potential visible light photocatalyst for pollutants degradation.

© 2016 Elsevier B.V. All rights reserved.

## 1. Introduction

Nowadays, in order to solve the serious energy and environmental crises accompanying the continuous industrial developments, people have to exploit new renewable and sustainable sources. The solar energy is a competitive candidate because of its cleanliness and sustainability. To make use of solar energy, photocatalyst is developed to drive a chemical process that can degrade organic pollutants [1] or convert the solar energy into other kinds of energy such as electric energy [2] and chemical energy [3–10]. For a certain photocatalyst, the photocatalytic performance strongly depends on its band structure, i.e., the band gap and energy levels of the conduction band (CB) and valence band (VB) to meet the optical absorption

and thermodynamic requirements [11]. Compared with single-component photocatalysts, heterostructure photocatalysts often display unique optical and electronic properties such as enhanced photoabsorption and charge transportation [12,13]. These advantages make heterostructures widely utilized in photocatalysis, e.g., the heterostructures of Bi<sub>2</sub>MoO<sub>6</sub>/TiO<sub>2</sub> [14], Ag<sub>3</sub>PO<sub>4</sub>/TiO<sub>2</sub> [15], H<sub>2</sub>WO<sub>4</sub>·H<sub>2</sub>O/Ag/AgCl [16], Ag<sub>2</sub>O/Bi<sub>2</sub>O<sub>2</sub>CO<sub>3</sub> [17], etc.

Among the numerous heterostructure photocatalysts, there are mainly two charge transfer modes. In one mode, the photogenerated electrons (e<sup>-</sup>) transfer to one semiconductor with more positive CB minimum (CBM) while holes (h<sup>+</sup>) transfer to one with more negative VB maximum (VBM). This mode can improve the charge-separation ability. However, it is unfavorable for the photocatalytic reaction because it leads to a lower height of reduction potential and higher height of oxidation potential [13]. In contrast, in the other mode, known as Z-scheme mode, the photogenerated electrons in one photocatalyst (*n*-type semiconductor) with a lower CBM recombine with the holes in the other photocatalyst (*p*-type semiconductor) with a higher VBM, facilitated by the electron mediator [11]. As a result, the strong oxidative holes

\* Corresponding author at: Department of Electronics and Key Laboratory of Photo-Electronic Thin Film Devices and Technology of Tianjin, Nankai University, Tianjin 300350, China.

\*\* Corresponding author.

E-mail addresses: [chengyahui@nankai.edu.cn](mailto:chengyahui@nankai.edu.cn) (Y.H. Cheng), [liuhui@nankai.edu.cn](mailto:liuhui@nankai.edu.cn) (H. Liu).

and strong reductive electrons are spatially separated to different semiconductors, and thus the whole system holds both the high charge-separation and strong redox ability. Because of these obvious advantages, the Z-scheme heterostructural photocatalysts have been considered as the most promising photoctalistic systems to date [18].

To construct a high efficiency Z-scheme photocatalyst, finding out an appropriate *p*-type semiconductor with high level of CBM is essential. The VBM of most oxide semiconductors are determined by O 2p orbits which is more positive than ca. +3.0 V vs. NHE [19], and the CBM is often more positive than the H<sup>+</sup>/H<sub>2</sub> potential (0 V vs. NHE). Thus most of narrow band oxide semiconductors are not conductive for the water reduction, and an all-solid-state Z-scheme photocatalyst is difficult to achieve. Nevertheless, cuprous oxide (Cu<sub>2</sub>O) is an exception. As a *p*-type semiconductor, Cu<sub>2</sub>O has a narrow direct band gap of 2.17 eV with much negative CBM (−1.4 V ∼ −0.3 V vs. NHE) [20–23]. Therefore, the photogenerated electrons in Cu<sub>2</sub>O can easily be captured to achieve photocatalysis [24]. Besides, as an important photocatalyst, Cu<sub>2</sub>O has more advantages like low cost, abundant resources, and non-toxicity [25–27]. However, the photocatalytic activity of Cu<sub>2</sub>O is very limit [28], and Cu<sub>2</sub>O has a poor stability in aqueous solution under light irradiation [23], which can easily be oxidized to CuO because of the lower VBM of Cu<sub>2</sub>O than the oxidation potential to CuO [13,25]. It is expected that the problems of instability and low photocatalytic activity may be solved by modifying Cu<sub>2</sub>O into proper heterostructure [11,13,29].

On the other hand, AgBr is an *n*-type semiconductor with the band gap of 2.6 eV [30], which has been extensively studied in photocatalysis and exhibited the outstanding photocatalytic activity [31–34]. By introducing noble metal Ag nanoparticles (NPs) to AgBr, the overall photocatalytic efficiency can be enhanced because of the surface plasmon resonance (SPR) and charge transfer [35,36]. However, AgBr is photosensitive materials, due to the presence of a large number of photogenerated electrons, the reduction of Ag<sup>+</sup> ions to Ag in AgBr is inevitable, reducing the stability of photocatalysts [34,37].

In this paper, to overcome the disadvantages of Cu<sub>2</sub>O, small amount of AgBr/Ag are used to modify the surface of Cu<sub>2</sub>O. It is found that by introducing non-precious metal Cu NPs between Cu<sub>2</sub>O and AgBr/Ag to form Z-scheme structure, the photocatalytic activity is improved significantly. More importantly, its stability is increased by the introduction of Cu NPs, and the photocatalytic efficiency remains steady during five cycles (90 min per cycle), indicating that both the oxidation of Cu<sub>2</sub>O and the decomposition of AgBr have been inhibited in the presence of Cu NPs. The photoelectrochemical (PEC) investigations indicate that the enhanced photocatalytic efficiency and stability are due to the improved charge separation originated from the Z-scheme structure.

## 2. Experimental

### 2.1. Chemicals and materials

Cupric sulfate (CuSO<sub>4</sub>·5H<sub>2</sub>O), sodium hydroxide (NaOH), ethylene glycol, hexadecyl trimethyl ammonium b romide (CTAB), triethanolamine (TEOA), hydrogen peroxide (H<sub>2</sub>O<sub>2</sub>) and isopropyl alcohol (IPA) were obtained from Tianjin Jiangtian Chemical Technology Co., Ltd., China. D-Glucose was provided by Tianjin Guangfu Technology Development Co., Ltd., China. Silver nitrate (AgNO<sub>3</sub>, 99.99%) and benzoquinone (BQ) were purchased from Sun Chemical Technology (Shanghai) Co., Ltd. All chemicals except AgNO<sub>3</sub> were of analytical grade and were used as received without further purification. Aqueous solutions were prepared using deionized water.

### 2.2. Synthesis of sphere Cu<sub>2</sub>O and Cu<sub>2</sub>O/Cu

The Cu<sub>2</sub>O and Cu<sub>2</sub>O/Cu with different Cu concentrations were synthesized following a facile redox procedure [38]. In a typical synthesis, 0.5 g of CuSO<sub>4</sub>·5H<sub>2</sub>O were dispersed in 20 mL of ethylene glycol and 10 mL of deionized water in a three-necked flask which was immersed in water bath at 60 °C. The mixture was stirred with a magnetic stirrer for about 10 min, and then 10 mL 5 M of NaOH was added dropwise. After 5 min of magnetic stirrer, 10 mL 1.1 M of D-glucose was added into the solution within 30 s. An orange-red colored precipitate ensued soon. The reaction was kept at 60 °C for 10 min. Afterwards, the product was centrifuged and washed with deionized water, and then dried at 60 °C for 3 h. To fabricate Cu<sub>2</sub>O/Cu, the reduction time was extended to 20 min, 40 min, 60 min and 180 min separately to obtain different content of Cu NPs. Other procedures were the same as that of Cu<sub>2</sub>O. The samples with different Cu reduction time were named as Cu\_20, Cu\_40, Cu\_60 and Cu\_180, respectively. According to our previous work, the mass percentage of Cu<sup>0</sup> in Cu<sub>2</sub>O/Cu\_40 is about 10.2% [39], i.e., the molar ratio of Cu<sup>+</sup> and Cu<sup>0</sup> is ca. 9:1.

### 2.3. Synthesis of heterostructural photocatalysts

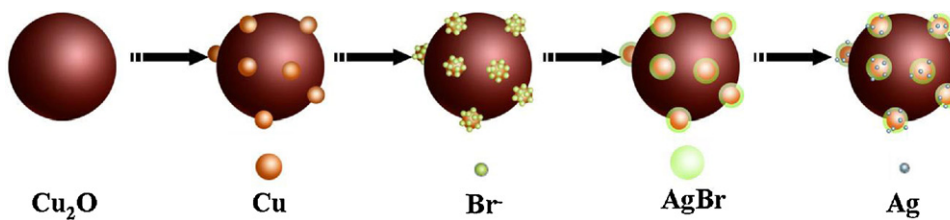
The obtained Cu<sub>2</sub>O or Cu<sub>2</sub>O/Cu samples (100 mg) were dissolved in 100 mL deionized water in the presence of CTAB (75 mg), and the solution was stirred for 60 min. Then 2.0 mL of 0.1 M AgNO<sub>3</sub> was added into the solution dropwise. During this process, the excessive surfactant CTAB absorbed onto the surface of Cu<sub>2</sub>O and induced Br<sup>−</sup> to react with Ag<sup>+</sup> to produce AgBr [36]. The entire experimental process was carried out in the dark. After 60 min of continuous stirring, the suspension was exposed to UV light to reduce Ag<sup>+</sup> to Ag<sup>0</sup> on the surface of AgBr. The UV-light irradiation time was adjusted for 10 min, 30 min and 60 min, respectively. The samples with different UV irradiation time are marked as Ag\_10, Ag\_30 and Ag\_60, respectively. At last, the obtained suspension was collected by centrifugation, washed with deionized water, and dried at 60 °C for 3 h. The forming mechanism of the Cu<sub>2</sub>O/Cu/AgBr/Ag photocatalyst is displayed in Scheme 1.

### 2.4. Characterization methods

The crystal structures were investigated using X-ray diffraction (XRD, D/max-2500) with Cu K $\alpha$  radiation ( $\lambda = 0.15406$  nm, 40 kV, 100 mA). Chemical components and valence states were analyzed by X-ray photoelectron spectroscopy (XPS, Thermo Escalab 250Xi) with Al K $\alpha$  X-ray source. The content of Ag and Cu was measured by inductively coupled plasma atomic emission spectrometry (ICP, Thermo X7). For all heterostructures, the molar ratio of elemental Cu and Ag is ca. 15:1, indicating a low content of Ag element. The morphologies and microstructures were characterized by scanning electron microscopy (SEM, SU 8010) and transmission electron microscopy (TEM, JEM-2010 FEF) operating at 200 kV. Optical absorption spectra were acquired with UV-vis spectrophotometer (Shimadzu 2600 PC) and UV-vis-NIR spectrophotometer (HITACHI UV-4100). Photoluminescence (PL) spectra were measured using a PL spectrophotometer (Horiba, FL-3-22) at room temperature.

### 2.5. Photocatalytic performance and electrochemical tests

Photocatalytic activities were evaluated by the photocatalytic decomposition of azo dye MO. Typically, 20 mg of photocatalyst was dispersed in 50 mL of 7 mg/L MO aqueous solution in a reactor condensed by the circulating water to keep the temperature unchanged. Prior to irradiation, the suspension was stirred in dark for 1 h to achieve an adsorption/desorption equilibrium of the dye



**Scheme 1.** Schematic illustration of formation of the  $\text{Cu}_2\text{O}/\text{Cu}/\text{AgBr}/\text{Ag}$  NPs.

molecules on the surface of the photocatalyst. After that, the suspension was illuminated under visible light ( $\lambda > 420 \text{ nm}$ ) by a 300 W Xe-arc lamp equipped with wavelength cutoff filters. At given time intervals, 3 mL of solution was centrifuged then the absorbance of the solution was measured. The degradation rate of dyes was calculated using the following equation,

$$D = (C_0 - C)/C_0 \times 100\% = (A_0 - A)/A_0 \times 100\%, \quad (1)$$

where  $A$  is the absorbency of the MO solution at 465 nm and  $C$  is the concentration of dye solution at different time intervals.

Additionally, the recycling experiments were performed to test the stability of photocatalysts. After each cycle, the catalyst was washed with deionized water and centrifuged, then dried at  $60^\circ\text{C}$  for 3 h.

The PEC property was measured using an electrochemical analyzer (PAP Versastat 4-200) in a standard three-electrode configuration. The photocatalyst sample was dip-coated onto the fluorine-doped tin oxide (FTO) transparent conductive film glass electrode and dried in air. The  $\text{Cu}_2\text{O}/\text{Cu}/\text{AgBr}/\text{Ag}$  coated FTO, Pt wire and  $\text{Ag}/\text{AgCl}$  (3.5 M KCl) were used as the working electrode, counter electrode, and reference electrode, respectively, and 0.1 M  $\text{Na}_2\text{SO}_4$  aqueous solution was used as the electrolyte. The PEC responses were measured under visible light ( $\lambda > 420 \text{ nm}$ ) and UV light ( $\lambda < 400 \text{ nm}$ ) using a 300 W Xe-arc lamp equipped with wavelength cutoff filters.

### 3. Results and discussion

#### 3.1. $\text{Cu}_2\text{O}/\text{AgBr}/\text{Ag}$ heterostructures

##### 3.1.1. Structure, morphology, and optical properties

Fig. 1a (i)–(iii) shows the XRD patterns of three typical samples, i.e., the  $\text{Cu}_2\text{O}/\text{AgBr}/\text{Ag}_{10}$ ,  $\text{AgBr}/\text{Ag}_{10}$  and  $\text{Cu}_2\text{O}$ . It is found that the diffraction peaks can be indexed into  $\text{Cu}_2\text{O}$  (JCPDS card No. 05-0667) and  $\text{AgBr}$  (JCPDS card No. 06-0438). No obvious diffraction peaks corresponding to elementary substance  $\text{Ag}$  can be observed, which is attributed to the low  $\text{Ag}$  content observed by the ICP measurements, as well as the small size of  $\text{Ag}$  particles [33]. To further verify the state of  $\text{Ag}$ , the microstructure and composition of the sample will be characterized by TEM and XPS later.

The morphologies of photocatalysts are investigated by SEM. Fig. 2a shows the SEM images of  $\text{Cu}_2\text{O}$  sample. It can be seen that the bare  $\text{Cu}_2\text{O}$  possesses perfect sphere structure with an average diameter of  $1.3 \mu\text{m}$ . In Fig. 2b–d, it shows that after modified by  $\text{AgBr}$ , the  $\text{Cu}_2\text{O}$  still maintain the original spherical morphology with the same average diameter. However, compared with the bare  $\text{Cu}_2\text{O}$ , it can be observed in Fig. 2b that some small spherical particles with the diameter of about  $100 \text{ nm}$  stick on the surface of  $\text{Cu}_2\text{O}$ . These nanoparticles can be identified as  $\text{AgBr}$ , which will be further proved by TEM images hereafter. Furthermore, as shown in Fig. 2c and d, after irradiated by UV light, some smaller NPs with diameters of  $12\text{--}25 \text{ nm}$  scatter over the surface of the samples. From the TEM analysis below, these smaller NPs are corresponding to the  $\text{Ag}$  NPs.

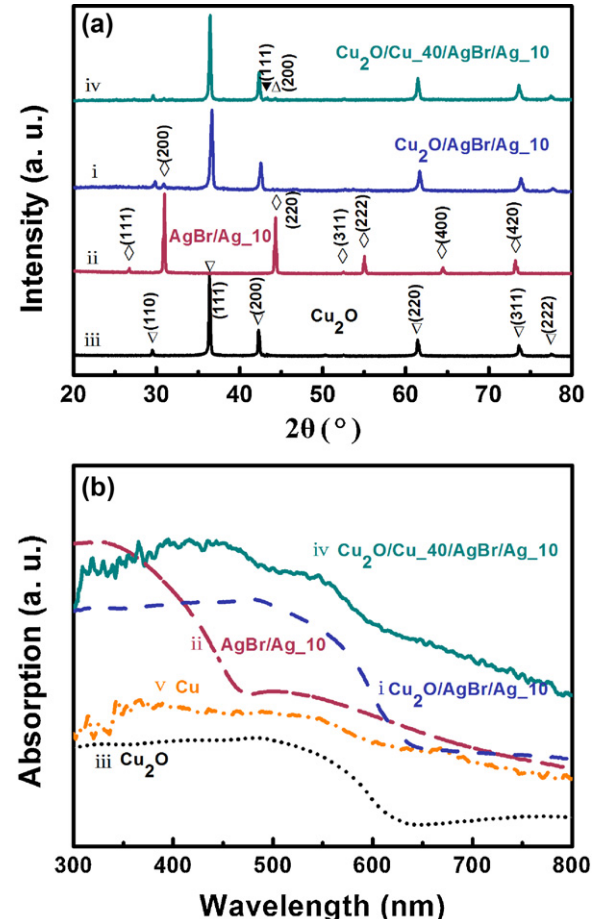


**Fig. 1.** (a) XRD patterns of different samples ( $\diamond$ :  $\text{AgBr}$ ,  $\nabla$ :  $\text{Cu}_2\text{O}$ ,  $\triangle$ :  $\text{Ag}$ ,  $\blacktriangledown$ :  $\text{Cu}$ ). (b) the UV-vis absorption spectra of different samples.

TEM bright field images of  $\text{Cu}_2\text{O}/\text{AgBr}/\text{Ag}_{10}$  were measured and shown in the insets of Fig. 2e and f. Besides, in order to clarify the microstructure and the component, the high resolution TEM (HRTEM) images of the selected areas are shown in Fig. 2e and f. In Fig. 2e, it is found that the spacing of adjacent lattice planes is ca.  $0.146 \text{ nm}$ ,  $0.288 \text{ nm}$  and  $0.204 \text{ nm}$ , which can be ascribed to the interplanar spacing of the (400), (200) and (220) planes of  $\text{AgBr}$ , respectively, indicating that the  $100 \text{ nm}$  NPs are composed of  $\text{AgBr}$ . In Fig. 2f, it is found that the spacing of adjacent lattice planes is ca.  $0.238 \text{ nm}$ , which can be ascribed to the interplanar spacing of the (111) planes of cubic  $\text{Ag}$ , indicating that the  $12\text{--}25 \text{ nm}$  NPs are mainly composed of  $\text{Ag}$ .

The optical properties of different photocatalysts were evaluated by UV-vis absorption spectroscopy. Fig. 1b (i)–(iii) shows the absorption spectra of  $\text{Cu}_2\text{O}/\text{AgBr}/\text{Ag}_{10}$ ,  $\text{AgBr}/\text{Ag}_{10}$  and  $\text{Cu}_2\text{O}$ , respectively. Bare  $\text{Cu}_2\text{O}$  has an absorption edge at the wavelength of about  $600 \text{ nm}$  and a maximum at around  $490 \text{ nm}$  corresponding to the band gap absorption of  $\text{Cu}_2\text{O}$  [29].  $\text{AgBr}/\text{Ag}$  has an absorption

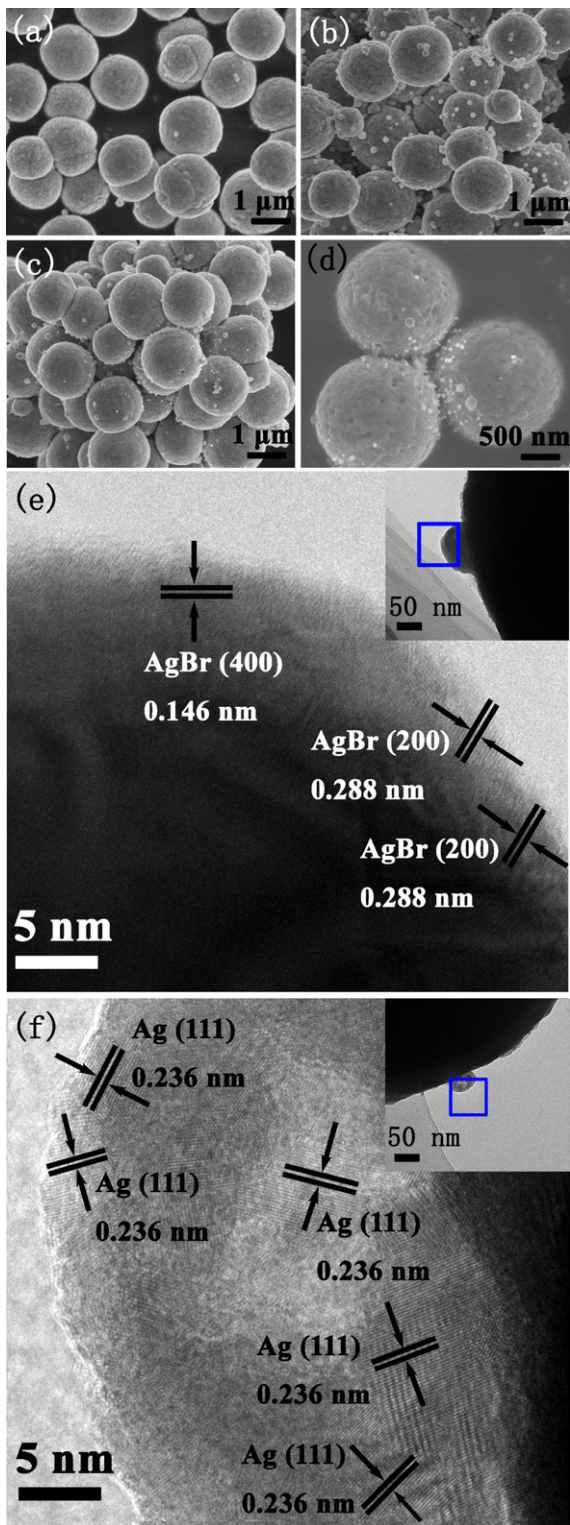


**Fig. 2.** SEM images of (a) Cu<sub>2</sub>O, (b) Cu<sub>2</sub>O/AgBr and (c), (d) Cu<sub>2</sub>O/AgBr/Ag.10. (e) and (f) TEM images of Cu<sub>2</sub>O/AgBr/Ag.10.

edge at about 480 nm, corresponding to the band gap absorption of AgBr [35]. Besides, AgBr/Ag sample shows a shoulder in the wavelength range of 480–800 nm, which can be attributed to the SPR effect of Ag NPs [40]. Due to the small amount of Ag NPs and the wide distribution of the particle size, the Ag SPR peak here is not sharp, which is in accordance with previous reports [35,41]. For Cu<sub>2</sub>O/AgBr/Ag.10, the relative absorption intensity in the wave-

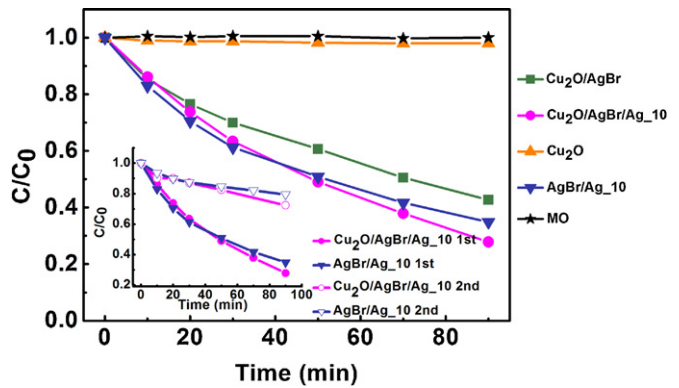


**Fig. 3.** Photocatalytic activities of Cu<sub>2</sub>O, AgBr/Ag.10, Cu<sub>2</sub>O/AgBr and Cu<sub>2</sub>O/AgBr/Ag.10 for MO degradation, and the self-degradation of MO under visible light irradiation. The inset is the cycling curves of AgBr/Ag.10 and Cu<sub>2</sub>O/AgBr/Ag.10 for MO under visible light irradiation.

length range of about 400–600 nm is greatly enhanced compared with the AgBr/Ag.10.

### 3.1.2. The photocatalytic activity and stability

Fig. 3 shows photodegradation of MO by different photocatalysts under visible light ( $\lambda > 420$  nm) illumination. The bare Cu<sub>2</sub>O is nearly invalid for degrading MO: only 2% MO is degraded within 90 min. When modified by AgBr, the degrading speed is improved: about 57% of MO is degraded within 90 min using Cu<sub>2</sub>O/AgBr, perhaps because of the superior photocatalysis activity of AgBr, as well as the improved carrier separation due to the heterostructure energy band structure. As such when introducing Ag on the surface of the photocatalysts, the degradation rate is further improved. About 72% of MO is degraded within 90 min in the existence of the Cu<sub>2</sub>O/AgBr/Ag.10, which is superior to Cu<sub>2</sub>O/AgBr due to the enhanced carriers separation capability caused by Ag. Moreover, the degradation rate over Cu<sub>2</sub>O/AgBr/Ag.10 is also higher than that of AgBr/Ag.10 as shown in Figs. 3 and S1 because of the improved carrier separation by forming the heterostructure.

The reaction kinetic studies indicate that the photodegradation of MO over all photocatalysts follows the pseudo-first-order kinetic model as Fig. S2 shown. The reaction rate constant ( $k$ ) is calculated using the formula of  $-\ln(C/C_0) = kt$ , where  $k$  is the kinetic constant and  $t$  is the reaction time. It also shows that Cu<sub>2</sub>O/AgBr/Ag.10 has the highest photodegradation rate compared with Cu<sub>2</sub>O, AgBr/Ag.10 and Cu<sub>2</sub>O/AgBr as mentioned above.

In order to study the stability of the Cu<sub>2</sub>O/AgBr/Ag samples in the photocatalytic process, the recycling experiments were performed. The inset of Fig. 3 shows the degradation curve of MO under visible light irradiation for the first and second cycle in the existence of AgBr/Ag.10 and Cu<sub>2</sub>O/AgBr/Ag.10. After irradiated for 90 min, MO degrades 72% and 28% separately for the first and second cycle for Cu<sub>2</sub>O/AgBr/Ag.10, and it is 65% and 20% separately for that of AgBr/Ag.10, indicating that the photocatalytic activity decreases markedly after one cycle of degradation for both two samples. To find out the reason of instability, the valence state evolutions of the samples before and after the photodegradation were further analyzed by XPS measurements. Fig. 4 shows the XPS spectrum of Ag 3d and Cu 2p state before and after the photocatalysis for the sample of Cu<sub>2</sub>O/AgBr/Ag.10. As shown in Fig. 4, the Ag 3d spectrum splits into Ag 3d<sub>5/2</sub> and Ag 3d<sub>3/2</sub> peaks, each of which can be fitted by two Gaussian functions. The peaks locating at the binding energy of ~367.9 eV and ~373.9 eV are contributed by Ag<sup>+</sup> in AgBr [41,42]. The peaks at the binding energy of ~368.6 eV and ~374.6 eV correspond to the Ag<sup>0</sup> [41], which manifests that the Ag NPs have really grown on the surface of photocatalysts. According to the areas of the fitted peaks, one can obtain the molar ratio of Ag<sup>+</sup> and Ag<sup>0</sup> to be

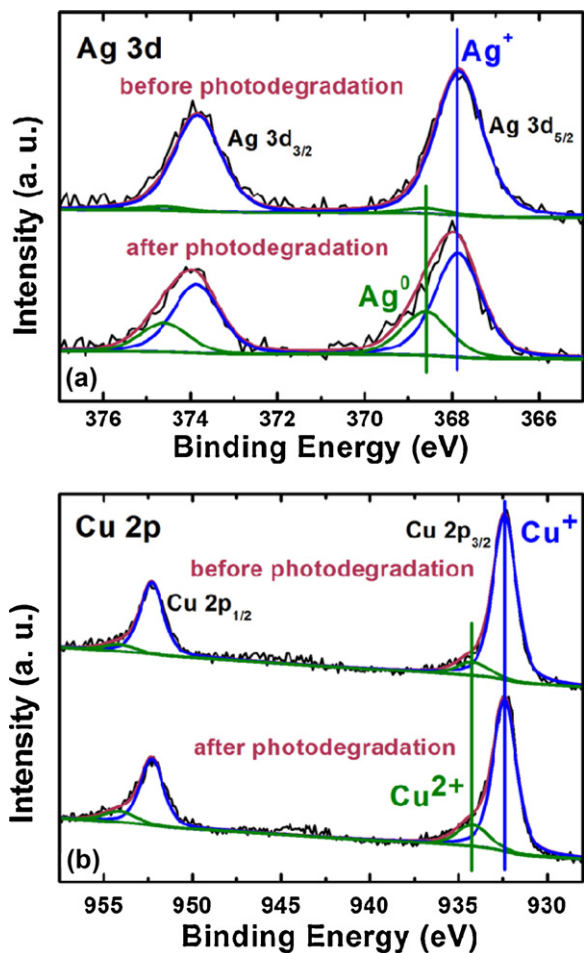


**Fig. 4.** (a) Ag 3d and (b) Cu 2p XPS spectra for the Cu<sub>2</sub>O/AgBr/Ag.10 sample before and after one cycle of degradation.

ca. 25:1. The relative area of the Ag<sup>0</sup> increases evidently after photodegradation, strongly suggesting the reduction of Ag<sup>+</sup> to Ag<sup>0</sup>. On the other hand, Cu 2p XPS spectrum also splits into two peaks, i.e., the Cu 2p<sub>3/2</sub> and Cu 2p<sub>1/2</sub> peaks. The Cu 2p<sub>1/2</sub> (950–957 eV) and Cu 2p<sub>3/2</sub> (930–937 eV) peaks both include the chemical states of Cu<sup>2+</sup> and Cu<sup>+</sup>. The peaks at ~952.3 eV and ~932.4 eV are characteristics of Cu<sup>+</sup> in Cu<sub>2</sub>O. The broadening parts of these two peaks, located at the binding energy of ~954.1 eV and ~934.2 eV separately, are related to the Cu<sup>2+</sup> in samples. It should be mentioned that for the as-prepared Cu<sub>2</sub>O, a small amount of CuO existing on the surface is inevitable. After the photocatalytic reaction, the relative area of the Cu<sup>2+</sup> peak increases obviously, indicating oxidation of Cu<sup>+</sup> during the photocatalysis. That is to say, the AgBr is decomposed to Ag and Cu<sub>2</sub>O is oxidized to CuO under the irradiation of visible light, which directly result in the decrease of the photocatalytic activity after one cycle photodegradation.

Besides, Cu<sub>2</sub>O/AgBr samples were also irradiated by UV light for 30 min and 60 min separately to prepare the Cu<sub>2</sub>O/AgBr/Ag.30 and Cu<sub>2</sub>O/AgBr/Ag.60 samples. In Fig. S3 in the Supplementary information, the XPS spectrum confirms that the relatively Ag<sup>0</sup> content increases evidently by extending the UV irradiation time from 10 min to 60 min. According to Fig. S3, Cu<sub>2</sub>O is also unstable under the UV light, that Cu<sup>+</sup> ions are greatly oxidized to Cu<sup>2+</sup> under irradiation. These results further prove that the Cu<sub>2</sub>O/AgBr/Ag systems are unstable under light. Under the irradiation, a large number of photogenerated electrons and holes can not be quickly consumed due to the poor carrier separating capacity. As a result, the excess photogenerated electrons of AgBr reduce Ag<sup>+</sup> ions into Ag<sup>0</sup>, and the

excess photogenerated holes of Cu<sub>2</sub>O oxidize Cu<sup>+</sup> ions into Cu<sup>2+</sup>. It will be seen in the next section that these results are totally different from the cases of containing metallic Cu.

### 3.2. Cu<sub>2</sub>O/Cu/AgBr/Ag

#### 3.2.1. Structure, morphology, and optical properties

According to the results above, it's crucial to prevent the corrosion of the Cu<sub>2</sub>O/AgBr/Ag photocatalysts to improve the stability. In this section, metallic Cu is introduced between Cu<sub>2</sub>O and AgBr, forming the Z-scheme heterostructure, to enhance the charge transfer and separation so as to improve the photocatalytic activity and stability. The Cu content was adjusted by changing the reduction time from 20 min to 60 min in preparation process, and the samples are denoted as Cu<sub>2</sub>O/Cu.20/AgBr/Ag.10, Cu<sub>2</sub>O/Cu.40/AgBr/Ag.10, and Cu<sub>2</sub>O/Cu.60/AgBr/Ag.10 (or referred as 20.CAA, 40.CAA, and 60.CAA), respectively. Fig. 1a (iv) shows the XRD patterns of the typical sample, i.e., Cu<sub>2</sub>O/Cu.40/AgBr/Ag.10 (40.CAA). It can be found that all diffraction peaks can be indexed into Cu<sub>2</sub>O (JCPDS card No. 05-0667), AgBr (JCPDS card No. 06-0438), and Cu (JCPDS card No. 04-0836). The detailed studies on the evolution and the content of Cu have been shown in our previous work [39]. Besides, the diffraction peaks of Ag are too weak to be observed.

Optical properties were studied by the absorption spectroscopy. Fig. 1b (iv) and (v) shows the absorption spectrum of Cu<sub>2</sub>O/Cu.40/AgBr/Ag.10 (40.CAA) and Cu.180, in which Cu.180 is mainly composed of Cu NPs [39]. By comparing 40.CAA with Cu<sub>2</sub>O/AgBr/Ag.10, it is found that after introducing Cu NPs, the visible light absorption of 550–800 nm enhances obviously, which may be caused by the absorption of Cu NPs [43,44]. In order to prove the enhanced absorption in 550–800 nm comes from Cu and show the absorption edge, we extend the absorption spectrum range of Cu<sub>2</sub>O/Cu.40/AgBr/Ag.10 and Cu (i.e. Cu.180) to the near infrared region as Supplementary information Fig. S4 shown. It is clear that both Cu<sub>2</sub>O/Cu.40/AgBr/Ag.10 and Cu exhibit an absorbance enhancement centered at the wavelength of ~560 nm, which has also been observed in other metallic Cu systems as a signature of SPR [39,44]. It should be noticed that the Cu absorption spectrum has a strong sloping background caused by the interband transitions [44], which mainly contribute to the absorption enhancement of Cu<sub>2</sub>O/Cu.40/AgBr/Ag.10 in the range of 600–800 nm.

Morphologies of the as-prepared Cu<sub>2</sub>O/Cu/AgBr/Ag samples were investigated by SEM. Fig. 5a and b shows the SEM images of two typical samples, i.e., Cu<sub>2</sub>O/Cu.40 and Cu<sub>2</sub>O/Cu.40/AgBr/Ag.10 (40.CAA), respectively. As revealed in Fig. 5a, some small Cu particles disperse on the surface of Cu<sub>2</sub>O, which have been analyzed in our previous work [39]. It should be mentioned that although the SEM images in Fig. 5a show that the particle size of Cu is around 200–300 nm, actually these particles are made up of a lot of smaller Cu particles with the average diameter of only about 20 nm as Fig. S5 (Supplementary information) shown [39]. In comparison, in Fig. 5b, it can be found that the size of Cu particles increases after introducing AgBr, suggesting that Cu particles were coated by AgBr. Obviously, the morphology of Cu<sub>2</sub>O/Cu/AgBr/Ag differs from that of Cu<sub>2</sub>O/AgBr/Ag due to the existence of Cu, which forms a connection between AgBr and Cu<sub>2</sub>O to constitute a Z-scheme system. Additionally, some smaller nanoparticles adhere to the surface of AgBr, which are attributed to Ag nanoparticles.

The TEM images of Cu<sub>2</sub>O/Cu.40/AgBr/Ag.10 samples were measured to further provide the microstructure information. To monitor the growth process of AgBr and prove the presence of Cu NPs, HRTEM images were recorded in different AgBr growth stages, including 10 min and 60 min, and are shown in Fig. 5. The inset of Fig. 5c shows the fast Fourier transform (FFT) patterns

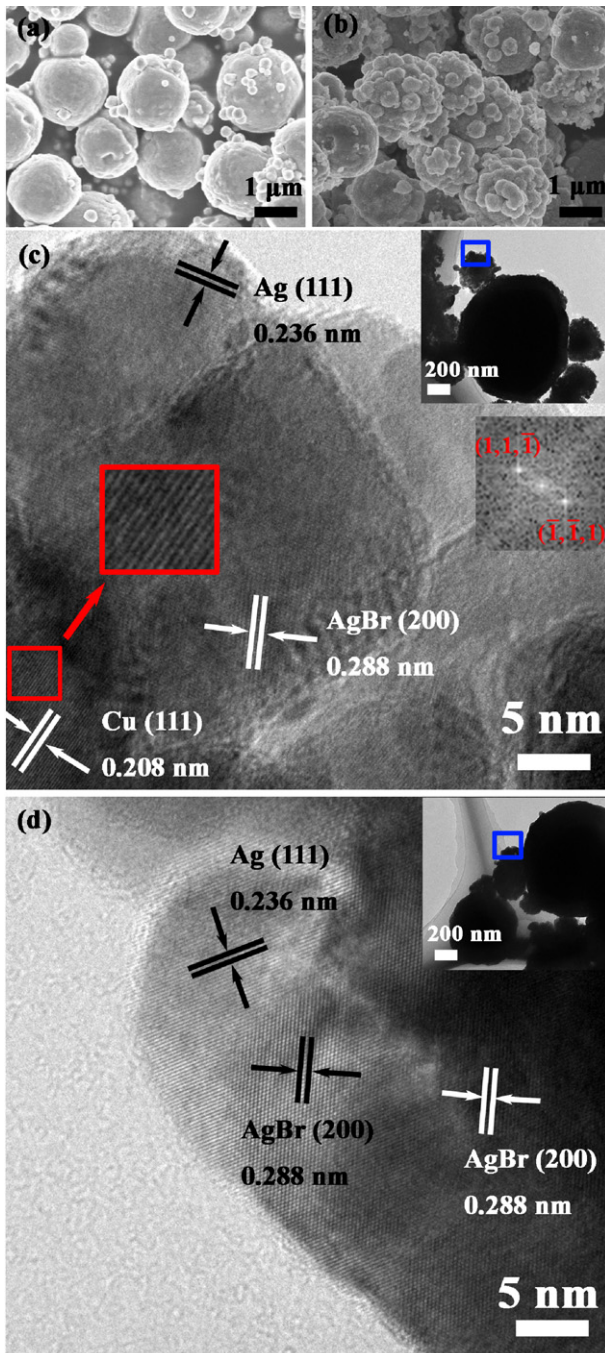


**Fig. 5.** SEM images of (a)  $\text{Cu}_2\text{O}/\text{Cu-}40$  and (b)  $\text{Cu}_2\text{O}/\text{Cu-}40/\text{AgBr/Ag-}10$ . (c) and (d) are TEM bright field images of  $\text{Cu}_2\text{O}/\text{Cu}/\text{AgBr/Ag}$  with the AgBr reaction time of 10 min and 60 min, respectively. The red square indicates the selected area for the fast Fourier transform. (For interpretation of the references to color in this figure legend, the reader is referred to the web version of this article.)

of the selected areas of each HRTEM images. Both Cu and AgBr can be clearly observed in the samples with the AgBr grown for 10 min, proving the presence of Cu. When the AgBr growth time extends to 60 min, the Cu crystal lattice disappears, and there is only AgBr phase which can be observed on the surface layer. From the XRD pattern and TEM images (with the reaction time of 10 min), it can be inferred that AgBr have covered Cu after a longer reaction time, and therefore metallic Cu locates between  $\text{Cu}_2\text{O}$  and AgBr.

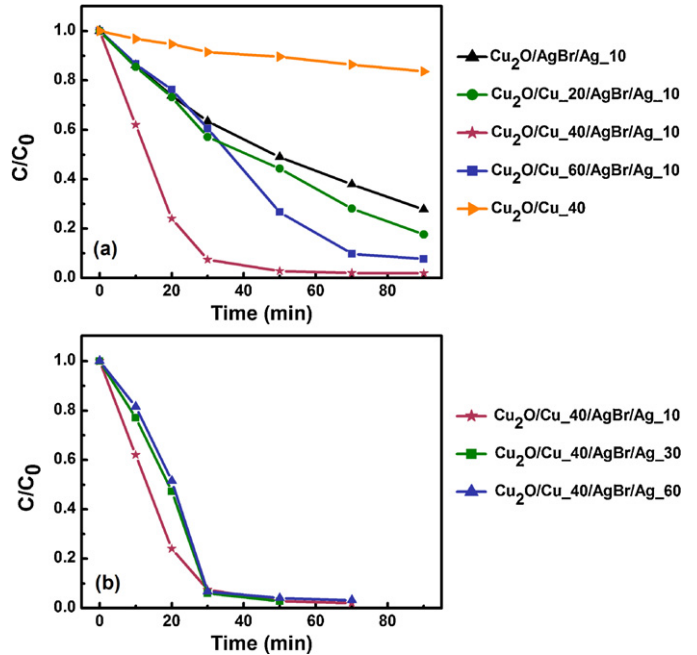


**Fig. 6.** Photocatalytic activities of  $\text{Cu}_2\text{O}/\text{Cu}/\text{AgBr/Ag}$  with (a) different reduction time and (b) different UV light irradiation time for MO degradation under visible light irradiation.

### 3.2.2. The photocatalytic activity and stability

Fig. S6 shows absorption spectrum of MO at various visible light irradiation times in the presence of 40.CAA (i.e.,  $\text{Cu}_2\text{O}/\text{Cu-}40/\text{AgBr/Ag-}10$ ). It can be seen that the MO has a sharp absorption peak at around 465 nm whose intensity reduces over the irradiation time. After irradiating for 30 min, the peak almost vanishes, suggesting that the MO is degraded. Photocatalytic performance of the samples with different Cu content was tested under visible light irradiation. As shown in Fig. 6a, the photocatalytic activity was enhanced significantly after Cu particles introduction. After irradiated under visible light for 50 min, the MO is degraded for 56%, 98%, and 73% in presence of 20.CAA, 40.CAA and 60.CAA, respectively. Remarkably, among all photocatalysts, 40.CAA (i.e.,  $\text{Cu}_2\text{O}/\text{Cu-}40/\text{AgBr/Ag-}10$ ) shows the highest photocatalytic activity, and the MO is degraded for 93% and 98% after 30 min and 50 min irradiation respectively, which is much better than  $\text{Cu}_2\text{O}/\text{AgBr/Ag-}10$  (51% for 50 min),  $\text{Cu}_2\text{O}$  (2% for 50 min) and  $\text{AgBr/Ag-}10$  (50% for 50 min) as shown in Fig. 3. The reaction rate constant  $k$  presented in Fig. S2 in the Supplementary information also indicates that 40.CAA has the best photocatalytic performance. The improvement of the photocatalytic activity mainly arises from the construction of Z-scheme heterostructure and the enhanced carriers' separation through the mediator of Cu. The SPR effect of Cu also contributes to the photocatalysis. However, by comparing the photocatalytic activity of these  $\text{Cu}_2\text{O}/\text{Cu}/\text{AgBr/Ag}$  samples with that of  $\text{Cu}_2\text{O}/\text{Cu-}40$  (10% for 50 min as shown in Fig. 6a), it can be found that the contribution of Cu SPR effect is not dominant. On the other hand, the amount of the Cu NPs increases with accumulating the reduction time, so the Cu coverage density increases gradually. Therefore, the absorption of  $\text{Cu}_2\text{O}$  gets weaker obviously [45]. Meanwhile, the contact surface of  $\text{Cu}_2\text{O}$  with the MO solution will also be reduced accordingly. All these factors have a negative influence on the photocatalytic activity of the  $\text{Cu}_2\text{O}/\text{Cu-}60/\text{AgBr/Ag-}10$  sample, so an appropriate content of Cu NPs is prerequisite.

As mentioned above, the stability of a photocatalyst is very important for its application. Fig. 7 shows the stability testing results of the  $\text{Cu}_2\text{O}/\text{Cu-}40/\text{AgBr/Ag-}10$  (40.CAA) sample. It can be seen that the photocatalytic activity keeps nearly unchanged for

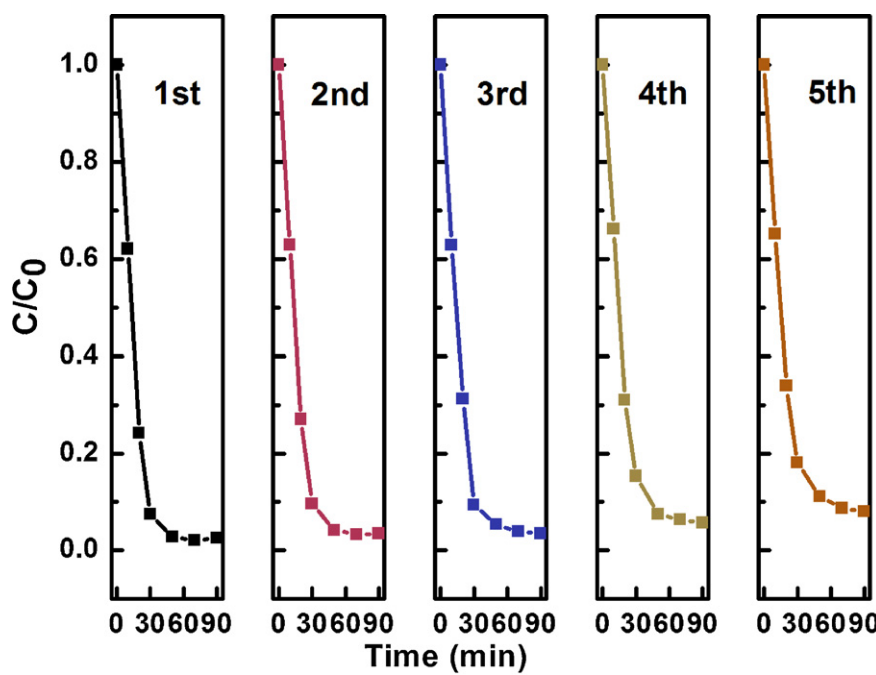


**Fig. 7.** The photodegradation curves for MO using  $\text{Cu}_2\text{O}/\text{Cu}_{.40}/\text{AgBr}/\text{Ag}_{.10}$  photocatalysts under visible light irradiation for five consecutive cycles.

5 cycles. The degrading rate for the fifth cycle is as high as 90% after irradiated for 50 min. In contrast, the photocatalytic activity of  $\text{Cu}_2\text{O}/\text{AgBr}/\text{Ag}_{.10}$  decreases to only 18% for the second cycle as shown in the inset of Fig. 3. It's obvious that the stability of the photocatalysts enhances significantly with the introduction of Cu.

The improvement of the stability can further be confirmed by the XPS measurements. Fig. 8 shows the XPS spectrum of Ag 3d and Cu 2p states of  $\text{Cu}_2\text{O}/\text{Cu}_{.40}/\text{AgBr}/\text{Ag}_{.10}$  before and after the photocatalysis. The relative areas of  $\text{Cu}^{2+}$  and  $\text{Ag}^0$  peaks have no obvious change, indicating no extra  $\text{Cu}^+$  (or  $\text{Cu}^0$ ) and  $\text{Ag}^+$  converted to  $\text{Cu}^{2+}$  and  $\text{Ag}^0$  during the photocatalysis. The results confirm that the components of  $\text{Cu}_2\text{O}/\text{Cu}_{.40}/\text{AgBr}/\text{Ag}_{.10}$  sample remain stable, which immediately result in its excellent photocatalytic stability for five cycles under visible light irradiation. It should be mentioned that the binding energies of  $\text{Cu}^+$  and  $\text{Cu}^0$  are 932.4 eV and 932.6 eV, respectively. The difference between two binding energies is only  $\sim 0.2$  eV, which is too small to be distinguished. So the peak at  $\sim 932.4$  eV may be attributed to the mixture of  $\text{Cu}^+$  and  $\text{Cu}^0$  here.

We have also studied the influence of UV irradiation on photocatalytic performance of the  $\text{Cu}_2\text{O}/\text{Cu}/\text{AgBr}/\text{Ag}$  samples. As shown in Fig. 6b, the photodegradation curves of samples with different UV irradiation time are coincide, suggesting that the amount of Ag doesn't change so much under UV irradiation. According to the XPS spectrum in Fig. S7, it is proved that both the amount of  $\text{Ag}^0$  and  $\text{Cu}^+$  is nearly unchanged, which indirectly demonstrates that the stability of  $\text{Cu}_2\text{O}/\text{Cu}/\text{AgBr}/\text{Ag}$  is improved significantly by introducing Cu NPs compared with the sample without Cu.

### 3.3. Possible photocatalytic mechanism

The  $\text{Cu}_2\text{O}/\text{Cu}_{.40}/\text{AgBr}/\text{Ag}_{.10}$  shows the highest photocatalytic activity, so we compare  $\text{Cu}_2\text{O}/\text{Cu}_{.40}/\text{AgBr}/\text{Ag}_{.10}$  with  $\text{Cu}_2\text{O}/\text{AgBr}/\text{Ag}_{.10}$ , which has the same content of Ag, to study the possible photocatalytic mechanism.

Firstly, to reveal the role of Cu in the photocatalysts, PL spectra of different samples were carried out and shown in Fig. S8 in the Supplementary information. For  $\text{Cu}_2\text{O}$ , under the excitation of 510 nm, an emission peak at  $\sim 580$  nm is observed relating to the direct

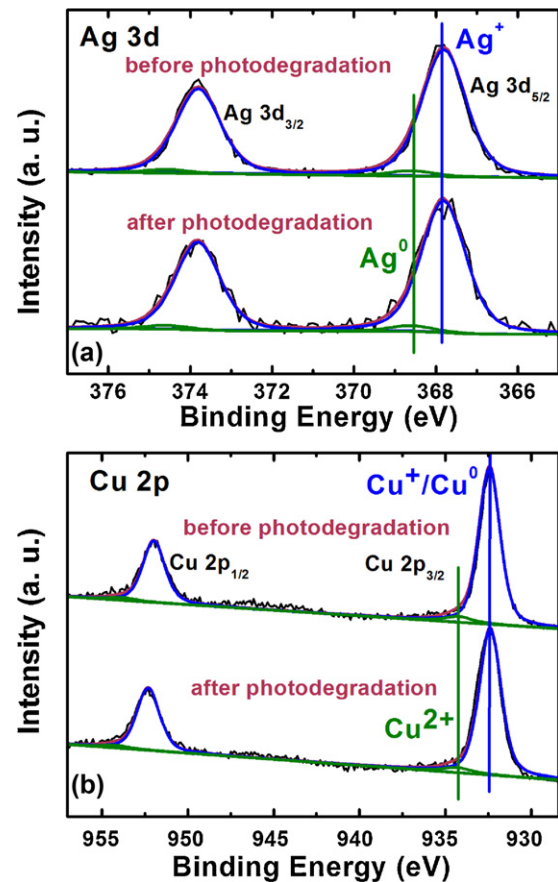


**Fig. 8.** (a) Ag 3d and (b) Cu 2p XPS spectra for the  $\text{Cu}_2\text{O}/\text{Cu}_{.40}/\text{AgBr}/\text{Ag}_{.10}$  sample before and after one cycle of degradation.

recombination of photogenerated electron-hole pairs of  $\text{Cu}_2\text{O}$ . While, for  $\text{AgBr}/\text{Ag}_{.10}$ , under the excitation of 325 nm, a strong emission peak at  $\sim 435$  nm is observed relating to the direct recombination of electron-hole pairs of  $\text{AgBr}$ . When combining  $\text{Cu}_2\text{O}$  and

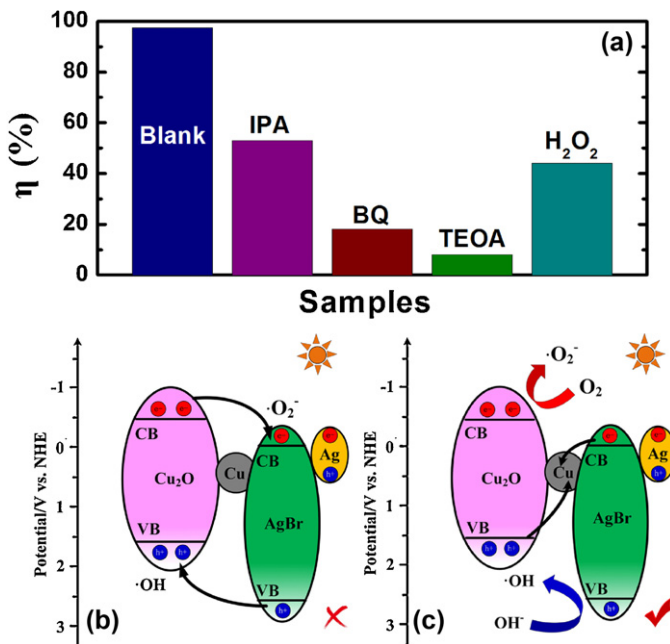
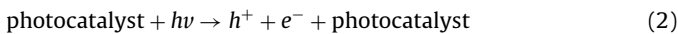


**Fig. 9.** (a) Photocatalytic degradation efficiency of MO over  $Cu_2O/Cu_{40}/AgBr/Ag_{10}$  in the blank and in the presence of IPA, BQ, TEOA and  $H_2O_2$ . (b) Heterojunction-type transfer and (c) Z-scheme mechanisms for the  $Cu_2O/Cu/AgBr/Ag$  system.

$AgBr/Ag_{10}$  together to form the hybrid structure, both two peaks are reduced by about 30%, indicating that the direct recombination of electron-hole pairs in both  $Cu_2O$  and  $AgBr$  is partially suppressed. Significantly, when Cu is introduced between  $Cu_2O$  and  $AgBr$ , all fluorescence emission peaks nearly disappear, indicating that the direct recombination of electron-hole pairs in both  $Cu_2O$  and  $AgBr$  has been almost completely inhibited [46,47]. These results indicate that Cu acts as an effective electron-hole transport mediator in the Z-scheme heterostructure for separating carriers. Besides, the results also indicate that although  $Cu_2O/AgBr/Ag_{10}$  can partially suppress direct recombination of carriers, this suppression is much weaker than in  $Cu_2O/Cu/AgBr/Ag$ .

The main active species of different photocatalysts may vary due to their different band structure and phase compositions, so the detection of active oxidant species is an indirect method to verify the photogenerated carriers transfer model [11,48]. Different scavengers used as probes are introduced during the photodegradation of MO under visible light irradiation. The scavengers include isopropanol (IPA) for  $•OH$  radicals, benzoquinone (BQ) for  $•O_2^-$  radicals, triethanolamine (TEOA) for holes and hydrogen peroxide ( $H_2O_2$ ) for electrons. As shown in Fig. 9a, the photocatalytic efficiency decreases obviously in the presence of IPA and BQ compared with that without scavengers, which suggests that  $•O_2^-$  and  $•OH$  are the main reactive species for MO degradation, which are produced by the following reactions [29]:



If the photogenerated charge carrier transfers between  $Cu_2O$  and  $AgBr$  via heterojunction-type transfer mechanism like Fig. 9b, the photogenerated holes might be accumulated in the VBM of  $Cu_2O$ . Because of the low potential of VBM of  $Cu_2O$ , the holes in the VB of  $Cu_2O$  could not oxidize  $OH^-$  into  $•OH$  with the oxidative potential of 2.6 V vs. NHE [45], which is not in agreement with the experimental results. In contrast, according to the Z-scheme mechanism in Fig. 9c, the holes are accumulated in the VB of  $AgBr$ , and

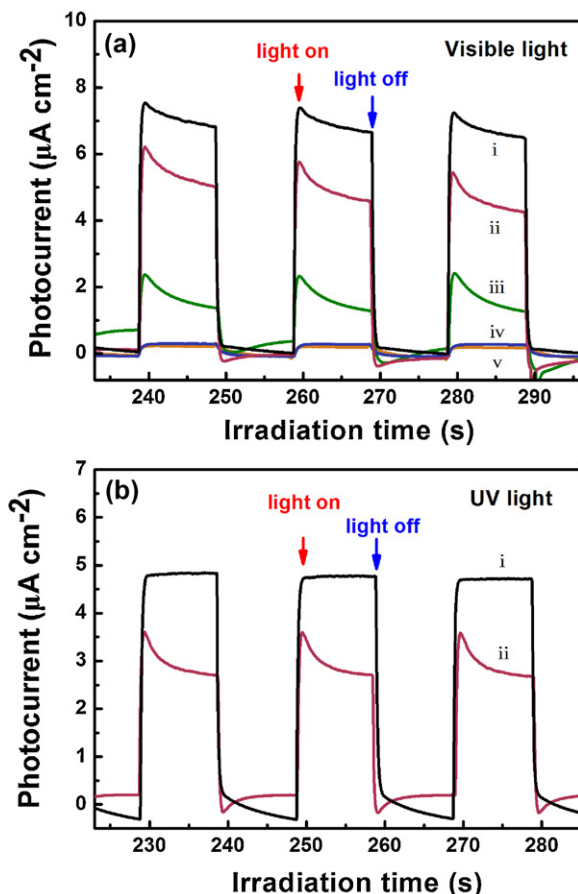


**Fig. 10.** Photocurrent responses for (i)  $Cu_2O/Cu_{40}/AgBr/Ag_{10}$ , (ii)  $Cu_2O/AgBr/Ag_{10}$ , (iii)  $Cu_2O/Cu_{40}$ , (iv)  $AgBr/Ag_{10}$  and (v)  $Cu_2O$  samples. (a) is under visible light and (b) is under UV light.

the photogenerated electrons are accumulated in the CB of  $Cu_2O$  respectively. The potential of VBM of  $AgBr$  is more positive than the oxidative potential of  $OH^-/•OH$ . Moreover,  $•O_2^-$  is easier to be produced due to the stronger reduction ability of the electrons in the CB of  $Cu_2O$ . Hence, the Z-scheme carrier transfer model is in agreement with the obtained experiment results.

When the hole scavenger TEOA is added into the solution, the photocatalytic efficiency ( $\eta$ ) decreases to only 8%. One reason is that the  $•OH$  radicals cannot be effectively produced if the holes are trapped on the basis of the reaction formula (3). Another reason is that according to Fig. 9b and c, the catch of holes will damage the Z-schematic charge transfer and may lead to other kinds of charge transfer, such as heterojunction-type transfer, which will hinder the production of  $•O_2^-$  radicals, thereby reducing the photocatalytic efficiency. When adding the electron scavenger  $H_2O_2$ ,  $\eta$  is 44%, which is higher than that of adding  $•O_2^-$  scavenger. This is reasonable because although the Z-schematic charge transfer is broken after adding  $H_2O_2$ , the  $H_2O_2$  can decompose into  $O_2$  and further reacts with electrons to produce  $•O_2^-$  [39].

To provide convincing evidence for the separation of photogenerated electron-hole pairs, photocurrent responses of  $Cu_2O$ ,  $Cu_2O/Cu$ ,  $AgBr/Ag_{10}$ ,  $Cu_2O/AgBr/Ag_{10}$  and  $Cu_2O/Cu_{40}/AgBr/Ag_{10}$  samples over several on-off irradiation cycles at 0 V vs.  $Ag/AgCl$  (3.5 M KCl) are recorded and shown in Fig. 10a. It's clear that the photocurrent densities decreased rapidly to zero as soon as the light is off, and the photocurrent density maintains stable value when the light is on.  $Cu_2O/Cu_{40}/AgBr/Ag_{10}$  produces a much higher photocurrent density than other samples under visible light, indicating a more efficient separation of

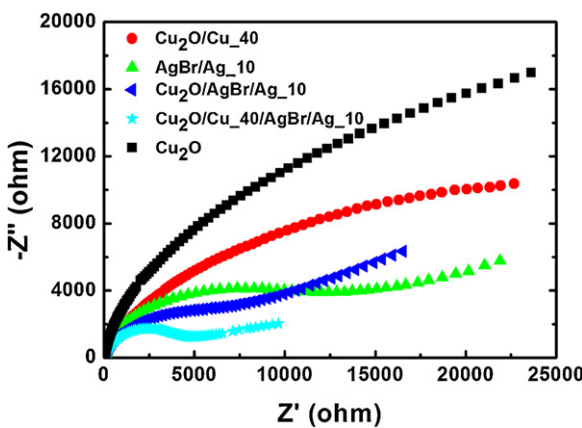


**Fig. 11.** The impedance measurement of different samples.

photogenerated carriers in  $\text{Cu}_2\text{O}/\text{Cu}_{.40}/\text{AgBr}/\text{Ag}_{.10}$ . The Fermi level of Cu sites at 4.65 V vs. vacuum level (i.e., +0.15 V vs. NHE) [49], forming the Ohmic contact with AgBr and  $\text{Cu}_2\text{O}$ . The photogenerated electrons at the CBM of AgBr can easily flow into Cu since the CBM potential of AgBr is more negative than the Fermi level of Cu (section 9 in Supplementary information). Then, the electron on the Fermi level of Cu transfer to the VBM of  $\text{Cu}_2\text{O}$  and recombine with the holes of  $\text{Cu}_2\text{O}$  quickly, which may be faster than the electron-hole recombination in the individual semiconductor [50], resulting the improvement of the charge carriers transfer and separation. Furthermore, the potential barrier seen by the electrons at the interface of the junction reflects electrons back into the  $\text{Cu}_2\text{O}$  NPs [50], which results in an increase of photocurrent. Meanwhile, the potential barrier also makes holes back into AgBr, so more holes can transform to  $\cdot\text{OH}$ , and a more efficiency oxidation reaction takes place. The results suggest that the introduction of Cu plays a key role on photocurrent. Besides, the transient current spikes can be observed, which may come from the accumulation and the recombination of photogenerated carriers at the photocatalyst-electrolyte interface [51].

It should be noticed that the enhanced light absorption may also play roles in photocurrent. Hence, in order to exclude the influence of Cu absorption on the photocurrent density, we measure the photocurrent responds of  $\text{Cu}_2\text{O}/\text{Cu}_{.40}/\text{AgBr}/\text{Ag}_{.10}$  and  $\text{Cu}_2\text{O}/\text{AgBr}/\text{Ag}_{.10}$  under UV light ( $\lambda < 400 \text{ nm}$ ) to avoid Cu SPR absorption. The results are shown in Fig. 10b. It is clear that when excluding Cu SPR effect, the photocurrent density of  $\text{Cu}_2\text{O}/\text{Cu}_{.40}/\text{AgBr}/\text{Ag}_{.10}$  ( $4.8 \mu\text{A}/\text{cm}^2$ ) is still higher than that of  $\text{Cu}_2\text{O}/\text{AgBr}/\text{Ag}_{.10}$  ( $2.8 \mu\text{A}/\text{cm}^2$ ), confirming the role of Cu is not only promoting the visible light absorption, but also increasing carrier separation.

Besides transient photocurrent, it's known that the radius of the arc on the electrochemical impedance spectroscopy (EIS) Nyquist plot reflects the reaction rate occurring at the surface of electrode and the smaller the arc radius represents the lower charge transfer resistance. As shown in Fig. 11, the introduction of Cu nanoparticles in the  $\text{Cu}_2\text{O}/\text{Cu}/\text{AgBr}/\text{Ag}$  sample leads to a significantly decreased arc radius of the semicircular Nyquist plot as compared with other samples, which also provide strong supports for the effective separation of electron-hole pairs.

Based on the above analyses, it is clear that the charge transfer for the  $\text{Cu}_2\text{O}/\text{Cu}/\text{AgBr}/\text{Ag}$  photocatalysts agrees well with the model shown in Fig. 9c and it is indeed a typical Z-scheme photocatalysts. The existence of Cu plays an important role in enhancing the photocatalytic efficiency and the stability of samples through the enhanced carrier transfer and separation. When introducing Cu between  $\text{Cu}_2\text{O}$  and AgBr, the Ohmic contact at the interface is formed, so that the photogenerated electrons in the CBM of AgBr

can easily transfer to Cu and then recombine with the photogenerated holes in the VBM of  $\text{Cu}_2\text{O}$  around the interface, improving the carrier separation. The residual photogenerated electrons in the CBM of  $\text{Cu}_2\text{O}$  and photogenerated holes in the VBM of AgBr can be used to realize photocatalytic reactions and realize strong redox capability. As a result, one can observe that the photodegradation speed of MO increased. Besides, because the instability of  $\text{Cu}_2\text{O}$  origins from the photogenerated holes which can oxidize  $\text{Cu}_2\text{O}$  into  $\text{CuO}$ , and the instability of AgBr origins from the photogenerated electrons which can reduce AgBr into Ag, these photogenerated carriers have recombined each other, so the stability of both  $\text{Cu}_2\text{O}$  and AgBr enhanced.

It should be noticed that if there is no Cu, the charge transfer mechanism is complicate in  $\text{Cu}_2\text{O}/\text{AgBr}/\text{Ag}_{.10}$ . The charge transfer in  $\text{Cu}_2\text{O}/\text{AgBr}/\text{Ag}_{.10}$  may improve the carrier separation. But its influence is very limited based on the fact that the differences in photodegradation rate among AgBr/Ag<sub>.10</sub>, Cu<sub>2</sub>O/AgBr and Cu<sub>2</sub>O/AgBr/Ag<sub>.10</sub> are small. Besides, according to the PL spectrum, it can be seen that there are still a large number of photogenerated carriers in semiconductors. These photogenerated carriers, especially the photogenerated carriers in AgBr, can realize the photocatalytic reaction. The accumulating of photogenerated electrons at the CBM of AgBr and the photogenerated holes at the VBM Cu<sub>2</sub>O will still reduce Ag<sup>+</sup> to Ag<sup>0</sup> and oxide Cu<sup>+</sup> to Cu<sup>2+</sup> to cause the system unstable.

At last, we compare the role of Ag with that of Cu. It is known that if Ag exists between Cu<sub>2</sub>O and AgBr, it can also act as the carrier mediator like Cu to improve the carrier separation. However, according to the SEM and TEM images in Figs. 2 and 5, it can be observed that most Ag NPs exist on the surface of the photocatalysts because Ag is obtained by photo-reduction of AgBr. In contrast, Cu is formed before the preparation of AgBr, so Cu lies between Cu<sub>2</sub>O and AgBr. Moreover, it can be observed in SEM and TEM images that if there is no Cu NPs, AgBr trends to stick on Cu<sub>2</sub>O as the sphere, and the contact area is small. After introducing Cu NPs, AgBr trends to coat on Cu NPs, thus the contact area increases greatly. But Ag particles cannot play such a role. Therefore the Cu NPs play a much more crucial role in Z-scheme than Ag NPs.

#### 4. Conclusions

$\text{Cu}_2\text{O}/\text{Cu}/\text{AgBr}/\text{Ag}$  photocatalyst has been successfully prepared through a two-step method. The photocatalysts containing Cu NPs show high photocatalytic activity for the degradation of MO under visible light. The MO is degraded for 98% after 50 min visible light irradiation in the existence of  $\text{Cu}_2\text{O}/\text{Cu}_{.40}/\text{AgBr}/\text{Ag}_{.10}$  photocatalyst, which is much better than that of the samples without Cu. The stability of the photocatalysts is also greatly improved when introducing Cu NPs between Cu<sub>2</sub>O and AgBr. The photocatalytic activity nearly keeps unchanged for 5 cycles and no extra Cu<sup>+</sup> and Ag<sup>+</sup> is transformed to Cu<sup>2+</sup> and Ag<sup>0</sup> during the photocatalysis process according to the XPS results. The Z-scheme transfer mechanism is confirmed by PL spectrum and the detection of active species. The enhanced properties are ascribed to the more efficient transfer and separation of photogenerated electron-hole pairs due to the presence of Cu NPs, which are proved by the photocurrent responses and the EIS Nyquist plots. These results demonstrate that the  $\text{Cu}_2\text{O}/\text{Cu}/\text{AgBr}/\text{Ag}$  is a potential visible light photocatalyst. In addition, the knowledge gained may provide deeper insights into the design of Z-scheme heterostructures.

#### Acknowledgements

The authors thank Prof. Dachi Yang for usage of his electrochemical workstation. This work was supported by the following grants:

National Basic Research Program of China (973 Program with No. 2014CB931703), National Natural Science Foundation of China (No. 51571123, 51101088, 51171082, 11304161, 51671108), and Tianjin Natural Science Foundation (No. 13JCQNJC02800, 13JCY-BJC41100, 14JCZDJC37700).

## Appendix A. Supplementary data

Supplementary data associated with this article can be found, in the online version, at <http://dx.doi.org/10.1016/j.apcatb.2016.10.086>.

## References

- [1] Y. Bi, S. Ouyang, N. Umezawa, J. Cao, J. Ye, *J. Am. Chem. Soc.* 133 (2011) 6490–6492.
- [2] J.A. Christians, R.C.M. Fung, P.V. Kamat, *J. Am. Chem. Soc.* 136 (2014) 758–764.
- [3] H. Tong, S. Ouyang, Y. Bi, N. Umezawa, M. Oshikiri, J. Ye, *Adv. Mater.* 24 (2012) 229–251.
- [4] M.G. Kibria, H.P.T. Nguyen, K. Cui, S. Zhao, D. Liu, H. Guo, M.L. Trudeau, S. Paradis, A.R. Hakima, Z. Mi, *ACS Nano* 7 (2013) 7886–7893.
- [5] S. Wang, W. Yao, J. Lin, Z. Ding, X. Wang, *Angew. Chem. Int. Ed.* 53 (2014) 1034–1038.
- [6] S. Wang, X. Wang, *Angew. Chem. Int. Ed.* 55 (2016) 2308–2320.
- [7] K. Maeda, K. Ishimaki, Y. Tokunaga, D. Lu, M. Eguchi, *Angew. Chem. Int. Ed.* 55 (2016) 8309–8313.
- [8] M. Jiang, Y. Gao, Z. Wang, Z. Ding, *Appl. Catal. B: Environ.* 198 (2016) 180–188.
- [9] S. Wang, Z. Ding, X. Wang, *Chem. Commun.* 51 (2015) 1517–1519.
- [10] S. Wang, X. Wang, *Small* 11 (2015) 3097–3112.
- [11] P. Zhou, J. Yu, M. Jaroniec, *Adv. Mater.* 26 (2014) 4920–4935.
- [12] D.J. Milliron, S.M. Hughes, Y. Cui, L. Manna, J. Li, L.W. Wang, A.P. Alivisatos, *Nature* 430 (2004) 190–195.
- [13] H.J. Li, Y. Zhou, W.G. Tu, J.H. Ye, Z.G. Zou, *Adv. Funct. Mater.* 25 (2015) 998–1013.
- [14] J. Tian, P. Hao, N. Wei, H.Z. Cui, H. Liu, *ACS Catal.* 5 (2015) 4530–4536.
- [15] M.Y. Zhang, L. Li, X.T. Zhang, *RSC Adv.* 5 (2015) 29693–29697.
- [16] X.F. Wang, S.F. Li, Y.Q. Ma, H.G. Yu, J.G. Yu, *J. Phys. Chem. C* 115 (2011) 14648–14655.
- [17] N. Liang, M. Wang, L. Jin, S.S. Huang, W.L. Chen, M. Xu, Q.Q. He, J.T. Zai, N.H. Fang, X.F. Qian, *ACS Appl. Mater. Interfaces* 6 (2014) 11698–11705.
- [18] H. Li, Y. Zhou, W. Tu, J. Ye, Z. Zhou, *Adv. Funct. Mater.* 25 (2015) 998–1013.
- [19] X. Chen, S. Shen, L. Guo, S.S. Mao, *Chem. Rev.* 110 (2010) 6503–6570.
- [20] L. Xiong, M. Ouyang, L. Yan, J. Li, M. Qiu, Y. Yu, *Chem. Lett.* 38 (2009) 1154–1155.
- [21] S. Wei, J. Shi, H. Ren, J. Li, Z. Shao, *J. Mol. Catal. A: Chem.* 378 (2013) 109–114.
- [22] M.I. Litter, *Appl. Catal. B: Environ.* 23 (1999) 89–114.
- [23] A. Paracchino, V. Laporte, K. Sivula, M. Gratzel, E. Thimsen, *Nat. Mater.* 10 (2011) 456–461.
- [24] L. Huang, F. Peng, H. Yu, H. Wang, *Solid State Sci.* 11 (2009) 129–138.
- [25] L. Liu, S.L. Lin, J.S. Hu, Y.H. Liang, W.Q. Cui, *Appl. Surf. Sci.* 330 (2015) 94–103.
- [26] Y.L. Pan, S.Z. Deng, L. Polavarapu, N.Y. Gao, P.Y. Yuan, C.H. Sow, Q.-H. Xu, *Langmuir* 28 (2012) 12304–12310.
- [27] L.X. Yang, S.L. Luo, Y. Li, Y. Xiao, Q. Kang, Q.Y. Cai, *Environ. Sci. Technol.* 44 (2010) 7641–7646.
- [28] C.-H. Kuo, C.-H. Chen, M.H. Huang, *J. Phys. Chem. C* 114 (2010) 5073–5079.
- [29] J.C. Wang, L. Zhang, W.X. Fang, J. Ren, Y.Y. Li, H.C. Yao, J.S. Wang, Z.J. Li, *ACS Appl. Mater. Interfaces* 7 (2015) 8631–8639.
- [30] N. Kakuta, N. Goto, H. Ohkita, T. Mizushima, *J. Phys. Chem. B* 103 (1999) 5917–5919.
- [31] X.F. Zhou, C. Hu, X.X. Hu, T.W. Peng, J.H. Qu, *J. Phys. Chem. C* 114 (2010) 2746–2750.
- [32] C.H. An, J.Z. Wang, C. Qin, W. Jiang, S.T. Wang, Y. Li, Q.H. Zhang, *J. Mater. Chem.* 22 (2012) 13153–13158.
- [33] W.S. Wang, H. Du, R.X. Wang, T. Wen, A.W. Xu, *Nanoscale* 5 (2013) 3315–3321.
- [34] X.X. Hu, X.F. Zhou, R. Wang, C. Hu, J.H. Qu, *Appl. Catal. B: Environ.* 154 (2014) 44–50.
- [35] P. Wang, B.B. Huang, X.Y. Zhang, X.Y. Qin, H. Jin, Y. Dai, Z.Y. Wang, J.Y. Wei, J. Zhan, S.Y. Wang, J.P. Wang, M.H. Whangbo, *Chem. Eur. J.* 15 (2009) 1821–1824.
- [36] Q. Yan, M. Sun, T. Yan, M.M. Li, L.G. Yan, D. Wei, B. Du, *RSC Adv.* 5 (2015) 17245–17252.
- [37] Y. Hou, X.Y. Li, Q.D. Zhao, X. Quan, G.H. Chen, *J. Mater. Chem.* 21 (2011) 18067–18076.
- [38] J. Kou, A. Saha, C.B. Stamper, R.S. Varma, *Chem. Commun.* 48 (2012) 5862–5864.
- [39] Y.H. Cheng, Y.J. Lin, J.P. Xu, J. He, T.Z. Wang, G.J. Yu, D.W. Shao, W.-H. Wang, F. Lu, L. Li, X.W. Du, W. Wang, H. Liu, R. Zheng, *Appl. Surf. Sci.* 366 (2016) 120–128.
- [40] C. Langhammer, Z. Yuan, I. Zoric, B. Kasemo, *Nano Lett.* 6 (2006) 833–838.
- [41] P. Wang, B.B. Huang, Z.Z. Lou, X.Y. Zhang, X.Y. Qin, Y. Dai, Z.K. Zheng, X.N. Wang, *Chem. Eur. J.* 16 (2010) 538–544.
- [42] M. Zhu, P. Chen, M. Liu, *ACS Nano* 5 (2011) 4529–4536.
- [43] K.P. Rice, E.J. Walker, M.P. Stoykovich, A.E. Saunders, *J. Phys. Chem. C* 115 (2011) 1793–1799.
- [44] A. Marimuthu, J. Zhang, S. Linic, *Science* 339 (2013) 1590–1593.
- [45] S. Pasternak, Y. Paz, *Chem. Phys. Chem.* 14 (2013) 2059–2070.
- [46] S. Wang, X. Wang, *Appl. Catal. B: Environ.* 162 (2015) 494–500.
- [47] S. Wang, J. Lin, X. Wang, *Phys. Chem. Chem. Phys.* 16 (2014) 14656–14660.
- [48] T. Arai, M. Yanagida, Y. Konishi, Y. Iwasaki, H. Sugihara, K. Sayama, *J. Phys. Chem. C* 111 (2007) 7574–7577.
- [49] O. Yamashita, *J. Appl. Phys.* 95 (2004) 178–183.
- [50] Y.J. Hwang, A. Boukai, P.D. Yang, *Nano Lett.* 9 (2009) 410–415.
- [51] A. Kargar, K. Sun, Y. Jing, C. Choi, H. Jeong, G.Y. Jung, S. Jin, D. Wang, *ACS Nano* 7 (2013) 9407–9415.